



Mapping the dynamics of eastern redcedar encroachment into grasslands during 1984–2010 through PALSAR and time series Landsat images



Jie Wang^a, Xiangming Xiao^{a,b,*}, Yuanwei Qin^a, Jinwei Dong^a, George Geissler^c, Geli Zhang^a, Nicholas Cejda^a, Brian Alikhani^a, Russell B. Dougherty^a

^a Department of Microbiology and Plant Biology, Center for Spatial Analysis, University of Oklahoma, Norman, OK 73019, USA

^b Institute of Biodiversity Science, Fudan University, Shanghai 200433, China

^c Oklahoma Forestry Services, Oklahoma Department of Agriculture, Food and Forestry, Oklahoma City, OK 73105, USA

ARTICLE INFO

Article history:

Received 30 May 2016

Received in revised form 27 November 2016

Accepted 30 December 2016

Available online xxx

Keywords:

Juniperus virginiana

Woody encroachment

Land cover

Phenology

Vegetation indices

ABSTRACT

Woody plant encroachment of eastern redcedar (*Juniperus virginiana* L., hereafter referred to as “red cedar”) into native grasslands in the U.S. Southern Great Plains has significantly affected the production of forage and livestock, wildlife habitats, as well as water, carbon, nutrient and biogeochemical cycles. However, time series of red cedar maps are still not available to document the continuously spatio-temporal dynamics of red cedar encroachment across landscape, watershed and regional scales. In this study, we developed a pixel and phenology-based mapping algorithm, and used it to analyze PALSAR mosaic data in 2010 and all the available Landsat 5/7 data during 1984–2010 with the Google Earth Engine (GEE) platform. This pilot study analyzed 4233 images covering > 10 counties in the central region of Oklahoma, and generated red cedar forest maps for 2010 and five historical time periods: the late 1980s (1984–1989), early 1990s (1990–1994), late 1990s (1995–1999), early 2000s (2000–2004), and late 2000s (2005–2010). The resultant maps for 2010, the late 2000s, early 2000s, and late 1990s were evaluated using validation samples collected from Google Earth’s high-resolution images and geo-referenced field photos. The overall (producer and user) accuracy of these maps ranged from 88% to 96% (88%–93%, and 96%–99%). The resultant maps clearly illustrated an increase in red cedar encroachment within the study area at an annual rate of ~8% during 1984–2010. These maps can be used to support additional studies on the driving factors and consequences of red cedar encroachment. This study also demonstrated the potential to trace the historical encroachment of red cedar into grasslands using time series Landsat images and PALSAR data.

© 2017 Elsevier Inc. All rights reserved.

1. Introduction

Woody plant encroachment has occurred globally across many ecosystems over the past century due to the effects of fire suppression, overgrazing, and climate changes (Archer et al., 1994; Barger et al., 2011; Van Auken, 2000). The Southern Great Plains (SGPs) of the US had five- to sevenfold greater woody plant expansion than other regions of the US (Zou et al., 2016), which was primarily caused by unregulated human settlement and livestock grazing (Hennessy et al., 1983; Inglis, 1964). More than 20 documented woody species have encroached into the grassland and savanna ecosystems of North America over the past century (Barger et al., 2011). Juniper encroachment mainly threatens the tall- and mixed-grass prairies of the Great Plains (Barger et al., 2011). In Oklahoma, *Juniperus virginiana* L. (eastern

redcedar) was reported to be encroaching into the grasslands and replacing the dominant oak trees in recent decades (DeSantis et al., 2010; Williams et al., 2013). The increased encroachment of eastern redcedar into native plant communities has threatened the sustainability, biodiversity, and productivity of native prairie ecosystems (Briggs et al., 2005; Engle et al., 1996). This shift in grassland species dominance has further affected ecosystem processes including water, carbon, nutrient, and biogeochemical cycles (Caterina et al., 2014; Williams et al., 2013; Zou et al., 2016).

Woody encroachment maps are vital for rangeland management, conservation planning, biodiversity assessment, and climate change studies. However, a time series of maps based on historically observed woody plant encroachment have not been produced at the regional scale (Gavier-Pizarro et al., 2012; Ge and Zou, 2013), the absence of which constrains our capacity to understand the ecological consequences, environmental impacts, and drivers of woody plant encroachment. For example, Ge and Zou (2013) simulated the impacts of eastern redcedar encroachment on regional climate in the SGPs. In their model simulation, the input maps of red cedar expansion were generated

* Corresponding author at: Department of Microbiology and Plant Biology, University of Oklahoma, 101 David L. Boren Blvd., Norman, Oklahoma 73019-5300, USA.

E-mail address: xiangming.xiao@ou.edu (X. Xiao).

URL: <http://www.eomf.ou.edu> (X. Xiao).

randomly, since the real maps of red cedar encroachment were not existent. In addition, the creation of regional-scale time series woody encroachment maps could reduce the uncertainty of continental-scale carbon budgets (Barger et al., 2011). Currently, it is hard to estimate the woody-plant expansion rate and describe the shapes of expansion curves for North America based on observations at two time points (Barger et al., 2011). Therefore, it is imperative to produce annual and multi-year maps of woody plant encroachment at regional and continental scales.

Traditional field survey approaches do not adequately document the expansive amount of data required to accurately map the spatio-temporal distribution and dynamics of woody plant encroachment at regional scales (Engle et al., 1996; Waser et al., 2008). Remote sensing images with long term data archives are alternative data sources to these studies. So far, most remote sensing studies have focused on (1) detecting trees in woodlands using very high spatial resolution (VHSR) aerial images (Anderson and Cobb, 2004; Poznanovic et al., 2014; Strand et al., 2006) and Lidar data (Falkowski et al., 2006), and (2) calculating the woody coverage in grasslands or savannas using multiple data sources, including Landsat Thematic Mapper/Enhanced Thematic Mapper Plus (TM/ETM+), radar, and Lidar (Sankey and Glenn, 2011; Urbazev et al., 2015; Yang et al., 2012). These studies were conducted at small spatial scales (e.g., rangeland or landscape) for a single year. Furthermore, no work has been established on mapping the encroaching species in grassland or savanna ecosystems over several decades.

The Landsat program has provided continuous Earth observation since the first satellite launch in 1972 (Wulder et al., 2012; Wulder et al., 2008). Images from Landsat TM, ETM+, and Operational Land Imager (OLI) have been recording continuous land cover changes with consistent spatial (30 m) and temporal (16 day) resolutions since 1984 (Wulder et al., 2016). An increasing number of land cover change studies have been conducted since the open access of the Landsat archive data in 2008 (Woodcock et al., 2008). However, optical remote sensing is sensitive to vegetation canopy (e.g., foliage cover), which may overestimate woody plant extent caused by the confusion with herbaceous vegetation or omit some woody plants with deciduous and semi-deciduous characteristics (Shimada et al., 2014). Synthetic Aperture Radar (SAR) sensors can penetrate clouds, and the longer wavelength SAR (L-band SAR) has better capability to obtain the vegetation structures (e.g., stem density, biomass.) (Baghdadi et al., 2009; Cloude and Papathanassiou, 2003). The great volume scattering from leaves, trunks, and branches provides promising signatures for the classification of forest coverage (Chen et al., 2016; Qin et al., 2015a; Shimada et al., 2014). The Advanced Land Observing Satellite (ALOS) Phased Array type L-band Synthetic Aperture Radar (PALSAR) was launched by the Japan Aerospace Exploration Agency (JAXA) in January 2006 and stopped operation in April 2011. It provided numerous data for forest (Qin et al., 2015a; Shimada et al., 2014) and plantation (Dong et al., 2013; Miettinen and Liew, 2011) mappings at the global and regional scales. Recent studies have shown that the combination of Landsat time series images and PALSAR data provides opportunities to monitor historical changes of forest resources (Lehmann et al., 2015).

The accuracy of land cover classification is impacted by both algorithms and remote sensing images (spatial, temporal and spectral resolutions). Broadband sensors have been widely used to generate regional or global land cover maps, which included vegetation types at the biome scale (Friedl et al., 2010; Gong et al., 2013; Loveland et al., 2000). Mapping at the plant species level has been mainly conducted using hyperspectral data with narrow bands (Clark et al., 2005; Martin et al., 1998) or VHSR images (IKONOS, WorldView-2, etc.) (Pu and Landry, 2012). Nevertheless, there are not sufficient amounts of hyperspectral and VHSR data for monitoring the long-term land cover changes at the species level. Several studies used time series images to track land surface phenology and generate land cover maps for crop species and forest plantations (Dong et al., 2013; Xiao et al., 2005; Zhong et al., 2014), and separate cropland and pasture in complicated savanna

landscapes (Mueller et al., 2015). These studies suggested the time series images can be used to extract seasonal, annual and multi-annual phenological indicators for plant species of interest. For example, time series Landsat images have been used to classify crop types and map rubber plantations by generating phenological metrics (Zhong et al., 2014) or selecting unique phenological windows (Dong et al., 2013) at regional scales. It is still unknown about the potential of 30 m Landsat images to recognize the species of trees (e.g., eastern redcedar) which has encroached into the grassland ecosystem.

This study intends to propose an approach to map the historical encroachment of eastern redcedar forest back to the 1980s by integrating PALSAR data in 2010 and long-term Landsat TM/ETM+ images during 1984–2010 using Google Earth Engine (GEE) cloud computing platform. Our three objectives were: (1) to develop a pixel and phenology-based algorithm to map the eastern redcedar encroachment into the grasslands based on PALSAR and Landsat time series images; (2) to quantify the dynamics of eastern redcedar encroachment by using remote sensing observations in five historical time periods of the late 1980s (1984–1989), early 1990 (1990–1994), late 1990s (1995–1999), early 2000s (2000–2004), and late 2000s (2005–2010); and (3) to quantitatively evaluate the recognition capability of moderate spatial resolution images of Landsat and PALSAR at the species scale using the pixel and phenology-based algorithm.

2. Material and methods

2.1. Study area

The study area (35°12'N–36°44'N, 96°25'W–98°59'W) covers >10 counties (~28,303 km²) across central and western Oklahoma (Fig. 1). It has a temperate continental climate. The annual mean air temperature is near 16 °C. The average annual precipitation is ~810 mm, and the northwestern regions are drier than the southeastern parts. The topography is generally flat with elevation ranging from 215 m to 612 m above sea level (Fig. S1a). The majority of this area is in the Central Great Plains ecoregion, with some small patches in the Cross Timbers and Flint Hills ecoregions (Fig. S1b) (Woods et al., 2005). Croplands, grasslands, and forests are the major land cover types, the combination of which accounted for about 90% of the study area. The spatial extent of urban areas were very small as captured on VHSR imagery dated 03/01/2011 from Google Earth (GE) (Fig. 1).

The study area is in the ecotone that connects the eastern deciduous forest and the tallgrass prairie, which includes a gradient from woody to non-woody vegetation (Hoagland, 2000; Myster, 2009). According to early vegetation investigations (Johnson and Risser, 1975), the latest Oklahoma Ecosystem Map (OKESM) (Diamond and Elliott, 2015), and our field survey in 2015 (Fig. 1), the deciduous forests in our study area are dominated by oaks, especially post oak (*Quercus stellata*) and blackjack oak (*Q. marilandica*). Eastern redcedar is the dominant evergreen species in forest and woodland/shrubland areas, while other evergreen tree species (e.g. pine) are few. In addition, bottomland hardwood forests (e.g., elms, pecan) can be seen along rivers or creeks. Eastern redcedar is evergreen without leaf color changes in fall. The species in post oak-blackjack and bottomland hardwood forests are deciduous types, which have seasonal leaf emergence and leaf fall (<http://www.forestry.ok.gov/ok-tree-guide>). The leaf phenology can be detected by time series optical remote sensing signals, which facilitates the separation of eastern redcedar forest from deciduous forests of oaks and other hardwood species.

Substantial eastern redcedar encroachment has occurred in this forest-prairie ecotone over the last several decades (Engle et al., 1996; Williams et al., 2013). Nearly no eastern redcedar was observed in the 1950s (Rice and Penfound, 1959). Forest surveys were conducted during the 2000s using standard dendrochronological methods covering our study area (DeSantis et al., 2011). The results showed that the eastern redcedar number increased from the 1960s to 1970s, and became

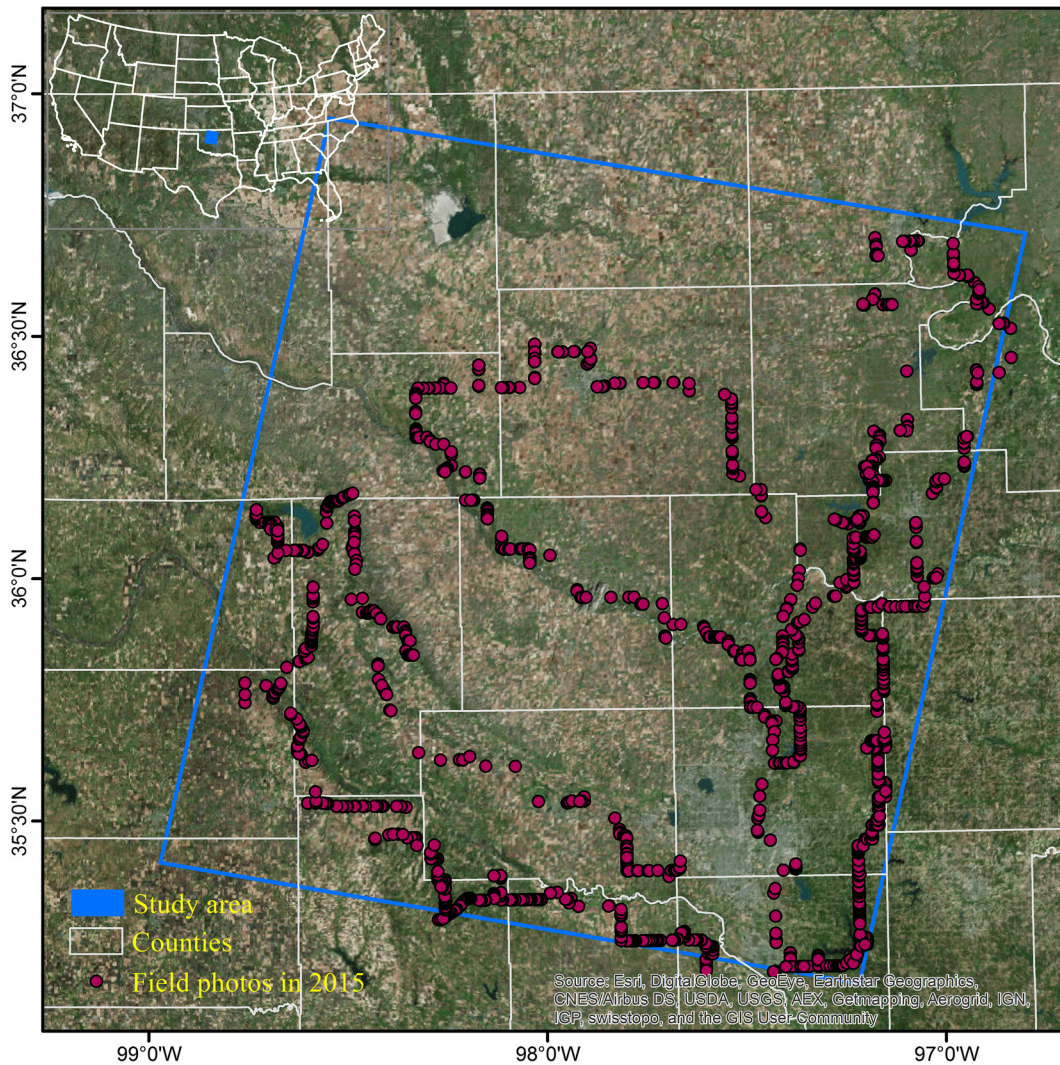


Fig. 1. The location of the study area and the counties it covers. A very high spatial resolution image dated 03/01/2011 from Google Earth and the field photos taken in 2015 are shown in this figure.

the primary recruitment species from the mid-1970s to the 2000s. Also, the eastern redcedar basal area increased from 0% to 43% and tree density increased from 2% to 56% between the 1950s to the 2000s (DeSantis et al., 2011).

2.2. Data

2.2.1. PALSAR data and pre-processing

The PALSAR datasets provided by the Earth Observation Research Center, JAXA, offer opportunities to develop forest maps at regional and global scales (Shimada et al., 2014). The 25 m PALSAR orthorectified mosaic datasets from 2007 to 2010 were generated from the annual HH and HV data acquired between June and October with Fine Beam Dual (FBD) polarization mode. The HH and HV data have been processed by geometric correction using a 90 m digital elevation model and radiometric calibration (Shimada et al., 2009; Shimada and Ohtaki, 2010). The mosaic data of HH and HV were expressed by gamma-naught (γ^0), due to the normalization of backscatter by the realistic illumination area (Shimada et al., 2014).

We downloaded all the 25 m PALSAR orthorectified mosaic data for Oklahoma in 2010. The Digital Number (DN) values (amplitude) of HH and HV were converted into backscattering coefficient (gamma-naught) in decibel using the following calibration coefficient (Shimada

et al., 2009).

$$\gamma^0 = 10 \times \log_{10} \langle DN^2 \rangle + CF$$

where γ^0 is the backscattering coefficient in decibel; DN is the digital number value of pixels in HH or HV; and CF is the absolute calibration factor of -83 .

2.2.2. Time series Landsat data and pre-processing

The GEE platform was used to collect and process all the Landsat images in this study. We used all the available standard U.S. Geological Survey Center (USGS) surface reflectance products of Landsat 5/7 covering the study area over Jan. 1984 to Mar. 2011, which have been collected in the GEE platform. The surface reflectance data was generated from the Landsat Ecosystem Disturbance Adaptive Processing System (LEDAPS), which includes the calibration from at-sensor radiance to the top of atmosphere (TOA) reflectance and the atmospheric correction from TOA reflectance to surface reflectance (Masek et al., 2006; Vermote et al., 1997). The study area is located within the Landsat scene of path/row 28/35. The pixels near the boundary of the study area had more observations due to the overlap of neighboring Landsat scenes (paths/rows of 27/35, 27/36, 28/34, 28/36, 29/34, 29/35). We constructed the 3-dimensional data cube of land surface reflectance using these seven overlapping Landsat scenes (a total of 4233 images). Fig. 2 shows the annual

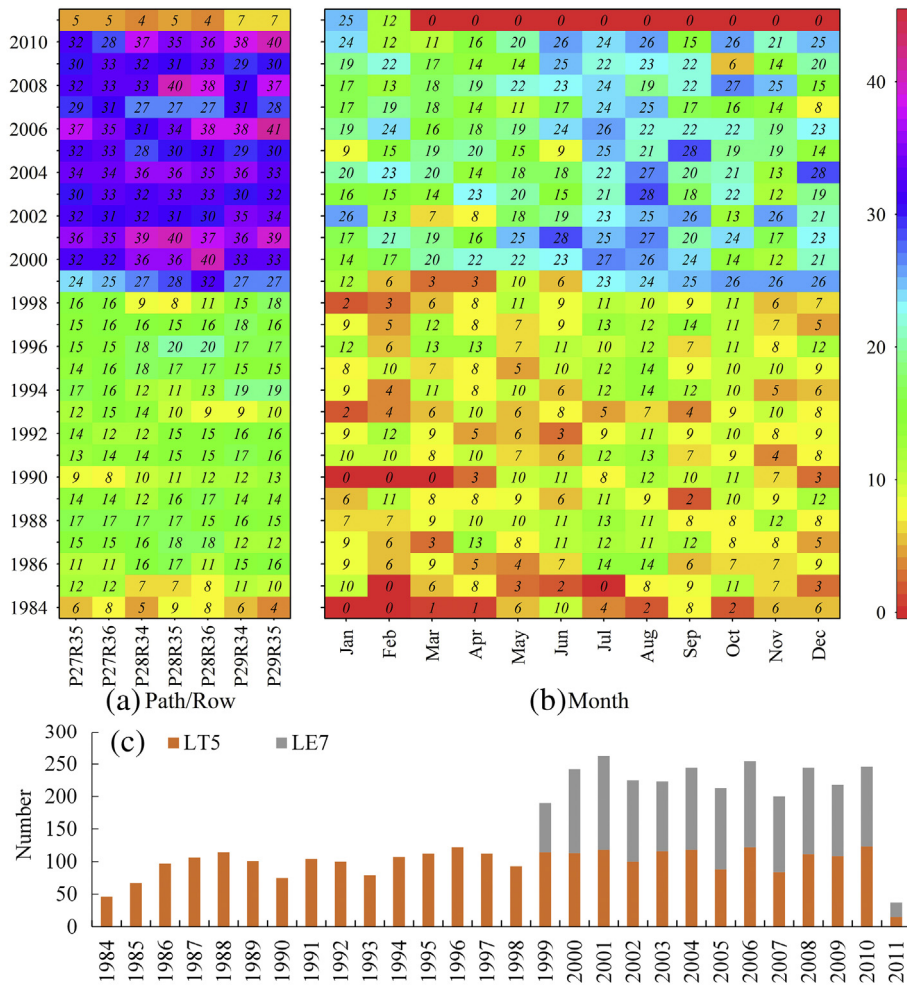


Fig. 2. The annual distribution of Landsat images used in this study. Statistics were conducted by (a) path/row, (b) month and (c) sensors.

distributions of all the available Landsat TM/ETM+ surface reflectance data over the study period by Landsat path/row (Fig. 2a), by months (Fig. 2b), and by sensors (Landsat 5/7) (Fig. 2c).

The quality of all observations for individual pixels in the data cube was assessed. The bad observations from clouds, cloud shadows, snow/ice and scan-line corrector (SLC)-off gaps were identified as NODATA according to the Fmask (Zhu and Woodcock, 2012) and metadata. Fmask had good performance to detect cloud and cloud shadows from Landsat 5/7 images with overall accuracy >90% (Zhu and Woodcock, 2012). The number of individual pixels from good Landsat 5/7 observations were counted during the winter (including Dec., Jan., and Feb.) for each year (Fig. S2). In 1984 and 1986, about 2% pixels in the study area had zero good observations in the winter season, while in the other years, all the pixels had at least one good observation during the winter (Fig. 3).

We calculated three vegetation indices (VIs) based on the surface reflectance data with good observations: Normalized Difference Vegetation Index (NDVI) (Tucker, 1979), Enhanced Vegetation Index (EVI) (Huete et al., 2002), and Land Surface Water Index (LSWI) (Xiao et al., 2005). NDVI and EVI are related to the vegetation greenness, and LSWI is sensitive to the vegetation water content. The times series data of these three VIs can be used to analyze the vegetation phenology (Huete et al., 2002; Xiao et al., 2006).

$$NDVI = \frac{\rho_{NIR} - \rho_{red}}{\rho_{NIR} + \rho_{red}} \tag{1}$$

$$EVI = 2.5 \times \frac{\rho_{NIR} - \rho_{red}}{\rho_{NIR} + 6 \times \rho_{red} - 7.5 \rho_{blue} + 1} \tag{2}$$

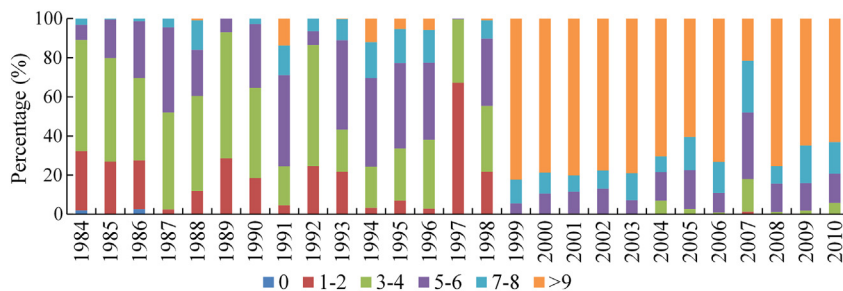


Fig. 3. Percentage of pixels with various good observation counts in the annual winter (Dec–Feb) from 1984 to 2010.

$$LSWI = \frac{\rho_{NIR} - \rho_{SWIR}}{\rho_{NIR} + \rho_{SWIR}} \quad (3)$$

where ρ_{blue} , ρ_{red} , ρ_{NIR} and ρ_{SWIR} are the surface reflectance values of blue (450–520 nm), red (630–690 nm), near-infrared (760–900 nm), and shortwave-infrared bands (1550–1750 nm).

2.2.3. Field survey data

Field surveys were carried out three times during November 7–21 in 2015 to collect ground reference data for training and validation samples. These field surveys mainly focused on the species (e.g. red cedar, oaks, and bottomland hardwoods) of forests and woodlands. We also noted other land cover types including shrubland, grassland, and cropland. The regions with large vegetation coverage were chosen as sampling sites. At each site, we took at least five photos with GPS cameras and recorded the vegetation characteristics (e.g. growth stage, composition of community). Field photos were taken following the rules described in-detail in previous publications (Qin et al., 2015b; Wang et al., 2015). Fig. 1 shows the distribution of the field photos, with a total number of 1970. These photos can be accessed freely at the global data portal at the Earth Observation and Modeling Facility (EOMF), University of Oklahoma (<http://www.eomf.ou.edu/photos/>) (Xiao et al., 2011). The training Region of Interests (ROIs) were digitized according to these field photos and the GE images during the winter and early spring over 2005–2010. Although the field photos were taken in 2015, they offered important references on vegetation types for the visual interpretation. We collected training ROIs stratified randomly across the red cedar and non red cedar forest areas (with plots/pixels of 46/11,712 for red cedar and 30/10,698 for other trees). The distributions of the training ROIs and the boundaries of all the used GE VHSR images are shown in Fig. S3. In this study, the phrase ‘other trees’ refers to those non red cedar species, mainly composed of oaks and bottomland hardwoods.

2.3. Algorithm to identify red cedar forest

Forest is defined as land (>0.5 ha) with tree canopy cover larger than 10% and minimum tree height of 5 m, according to the United Nations Food and Agriculture Organization (FAO) (FAO, 2012). The workflow for mapping long-term (1984–2010) red cedar forest included three sections (Fig. 4). First, a baseline forest map in 2010 was produced using a decision tree algorithm based on 25 m 2010 PALSAR data.

Second, the 2010 red cedar forest map was produced using a pixel and phenology-based algorithm based on the 2010 forest map and the Landsat images in the winter of 2010 (Dec. 2010–Feb. 2011). Finally, a red cedar forest stand-age map in 2010 was produced based on the historical red cedar forest maps. The historical red cedar forest distributions were generated based on the 2010 forest map and Landsat times series images in 1984–2010 using the pixel and phenology-based algorithm. The red cedar forest maps were produced for the late 1980s (1984–1989), early 1990s (1990–1994), late 1990s (1995–1999), early 2000s (2000–2004) and late 2000s (2005–2010). The detailed workflow is described in the following paragraphs.

2.3.1. Phenology and signature analysis of red cedar and non red cedar forests

We selected three sites (Fig. S4a) with a largely homogeneous vegetation extent that represented red cedar, oak and bottomland hardwood forest types, according to the landscapes from the GE images and the field photos (Fig. S4b–g). Time series of three VIs (NDVI, EVI and LSWI) at these three sites were created using Landsat 5/7 data from 2005 to 2011 to examine the phenological characteristics of the forest types (Fig. 5). Oak and bottomland hardwood forests had more significant seasonal variations in the three VIs than did the evergreen red cedar forest. In comparison, red cedar forest had significantly lower VIs in summer and higher VIs in winter, which suggests the potential to separate red cedar forest from other forest types. In winter, NDVI and LSWI showed larger differences between red cedar and other forest types than EVI did. However, LSWI tended to be influenced by ice and/or snow cover, which have a higher reflectance in the visible and near infrared bands than vegetation (Xiao et al., 2004).

To map the red cedar at regional scale over multiple years, we analyzed the seasonal characteristics of NDVI based on the training ROIs of red cedar (11,712 pixels) and other trees (10,698 pixels) over a period of 2005–2010. We calculated the monthly mean NDVI (NDVImean) for individual pixels based on the Landsat 5/7 NDVI time series with a 8-day interval. We analyzed the mean values and standard deviations of monthly NDVImean for all the pixels of red cedar and non red cedar forests, in each year (Fig. S5) and in multiple years together over 2005–2010 (Fig. 6). The comparison of monthly NDVImean in summer and in winter suggested NDVImean in winter has a better ability to separate red cedar trees from other trees, as the monthly NDVImean of red cedar forests in winter was much higher than that of other forest types. These results also suggested that a threshold of about 0.4 can be used to extract the red cedar forest based on the winter NDVImean.

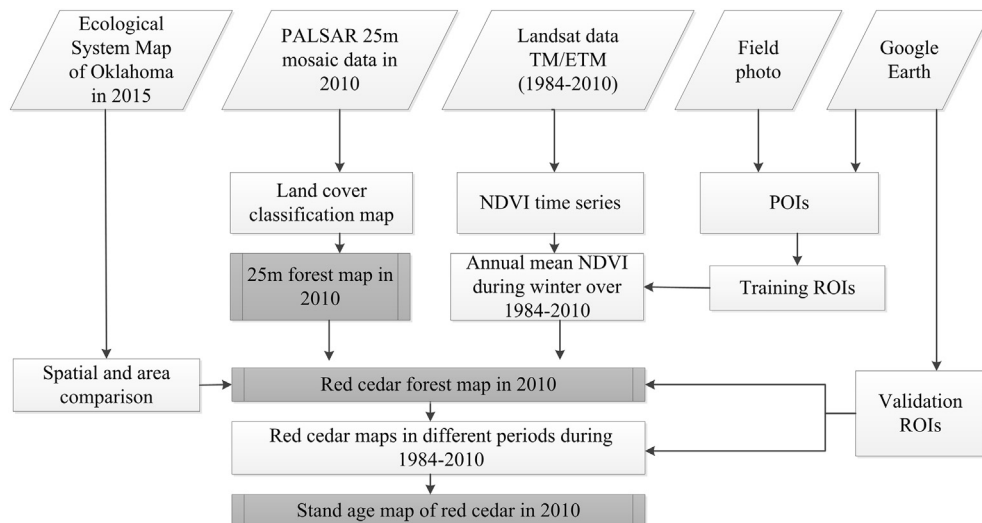


Fig. 4. Workflow of red cedar forest mapping using 25 m PALSAR mosaic data in 2010 and Landsat time-series images over 1984–2010. A detailed workflow for forest mapping was shown in previous publication (Qin et al., 2016a). (For interpretation of the references to color in this figure legend, the reader is referred to the web version of this article.)

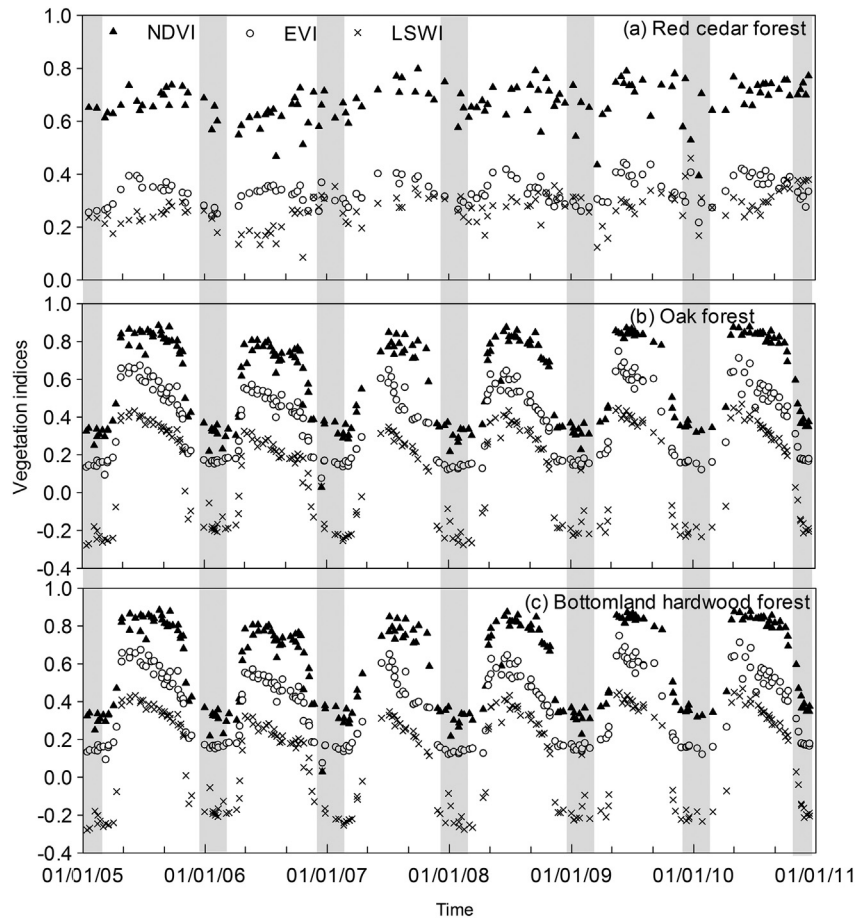


Fig. 5. Seasonal and interannual variations of Landsat (TM/ETM+)–derived vegetation indices (NDVI, EVI and LSWI) for forest samples of (a) red cedar, (b) oak and (c) bottomland hardwood during 2005–2010. The winter in each year were delineated by grey boxes. The landscapes of these forest samples were shown in Fig. S4. (For interpretation of the references to color in this figure legend, the reader is referred to the web version of this article.)

To confirm this information, we analyzed the signature distribution in HH, HV, and NDVImean in summer and in winter based on 2010 PALSAR data, 2010 Landsat 5/7 NDVI time series, and training ROIs of red cedar and non red cedar forests (Fig. 7). Fig. S6 shows these individual images and their spectral data. Red cedar and non red cedar forests had similar backscatter signature in PALSAR HH and HV, which can be used to extract a boundary of forests mixed with red cedar and non red cedar. In contrast, the spectral signature from NDVImean in summer and in winter showed some differences between red cedar and non

cedar forests. NDVImean in winter had the maximum between-class variance, which had the highest discrimination ability. Statistical analysis showed that using a threshold of 0.40 can separate 95% of red cedar pixels (>0.4) from 99% of the pixels of non red cedar forest (<0.4) (Fig. 7d).

2.3.2. Algorithm of red cedar forest mapping

We have developed a decision classification algorithm for mapping forest based on 50 m PALSAR mosaic data (Dong et al., 2012a), the integrated data of 50 m PALSAR and MODIS (Qin et al., 2015a; Qin et al., 2016b), and the integrated data of 25 m PALSAR and Landsat images (Chen et al., 2016). Previous studies showed forests, water, cropland, and other land cover types had different backscatter signature in HH, HV, HH/HV (Ratio), and HH-HV (Difference), which can be used to identify these land cover types (Chen et al., 2016; Dong et al., 2012a; Dong et al., 2012b; Qin et al., 2015a). We recalculated the frequency distributions of HH, HV, HH/HV and HH-HV for five main land cover types in this area (Fig. S7), based on 25 m PALSAR data in 2010 and land cover samples (Fig. S8). To generate a forest and non-forest map, this study followed the PALSAR-based forest mapping algorithm using 25 m PALSAR mosaic data in 2010 with updated thresholds of $-16 < HV < -8$ & $2 < \text{Difference} < 8$ & $0.3 < \text{Ratio} < 0.85$ (Qin et al., 2016a). Then, this PALSAR-based 25 m forest map in 2010 was resampled to 30 m to match Landsat spatial resolution. This forest map composed by red cedar and non red cedar types provided a baseline forest mask to overlay with the phenology characteristics from the time series Landsat data for the red cedar forest mapping.

A pixel and phenology-based algorithm was developed to map the red cedar forest in 2010 and five historical time periods. According to

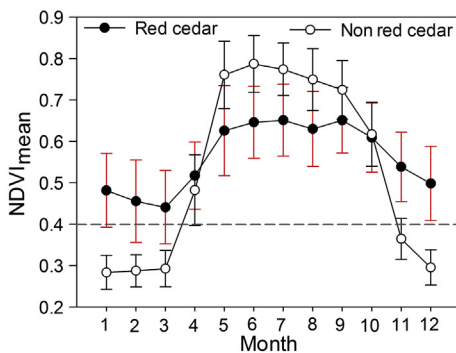


Fig. 6. The monthly mean and standard deviation (SD) of NDVI of red cedar and non red cedar forests. These values were calculated based on the training ROIs over years of 2005–2010. The monthly mean and SD of NDVI of red cedar and non red cedar forests for individual years during 2005–2010 were shown in Fig. S5. (For interpretation of the references to color in this figure legend, the reader is referred to the web version of this article.)

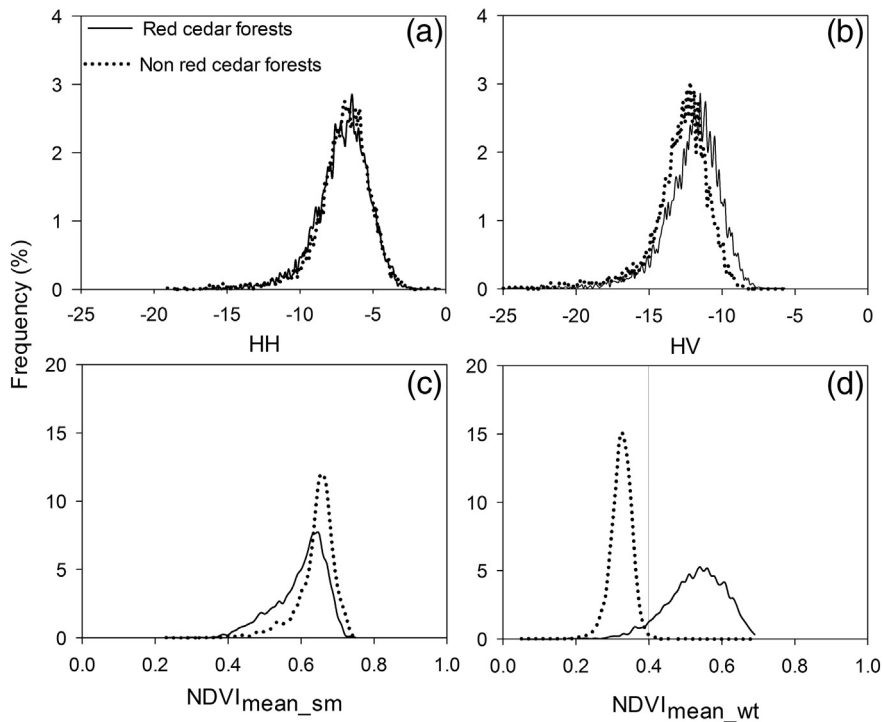


Fig. 7. Frequency histograms of red cedar and non red cedar forests in 25 m 2010 PALSAR (a) HH, (b) HV bands, and in the mean NDVI during the (c) summer and (d) winter of 2010. The solid line in (d) shows the threshold of 0.4 separating 95% of the red cedar pixels from 99% of the pixels of non red cedar forests. The statistics were based on the training regions of interests (ROIs) of red cedar and non red cedar forests. (For interpretation of the references to color in this figure legend, the reader is referred to the web version of this article.)

the analysis in Section 2.3.1, Landsat images in winter were used to calculate the NDVI time series and generate the mean NDVI map in winter. The mean NDVI in winter larger than 0.4 was used to separate red cedar forest from other forest types.

In summary, we first produced the red cedar forest map in 2010 based on the 25 m PALSAR data in 2010 and the Landsat-derived NDVI time series in the winter of 2010 using the rules of (1) $-16 < HV < -8$, and $2 < \text{Difference} < 8$, and $0.3 < \text{Ratio} < 0.85$, and (2) the winter $\text{NDVImean} > 0.4$. Second, following these rules, we produced the annual red cedar maps over 1984–2009 based on the 2010 PALSAR data and the annual time series Landsat data in the winter. Then, the annual red cedar maps were combined into 5 historical time periods using frequency combination to reduce the uncertainties caused by image quality or other factors. The 5 time periods were defined with 5 or 6 years as a group, including the late 1980s (1984–1989), early 1990s (1990–1994), late 1990s (1995–1999), early 2000s (2000–2004) and late 2000s (2005–2010). During each time period, we counted the number of individual pixels identified as red cedar based on the annual red cedar maps. A pixel with a number ≥ 3 (frequency $\geq 50\%$) was identified as red cedar. Third, the stand-age map of red cedar forest in 2010 was produced by examining the first red cedar occurrence time for individual pixels based on the red cedar map in 2010 and the maps in five historical time periods. In this study, the 2010 PALSAR data was used to trace back the historical red cedar distribution, as long-term PALSAR data did not yet exist. We assumed that the 2010 PALSAR data provided the maximum red cedar distribution during 1984–2010, because the red cedar has encroached continuously into Oklahoma grasslands during recent decades (Williams et al., 2013; Zou et al., 2016).

2.4. Accuracy assessment of red cedar forest maps

A stratified random sampling design was used to acquire validation samples to estimate the accuracies of the red cedar forest maps. We stratified two classes of red cedar and non red cedar forests. Good practices for assessing accuracy of land cover changes suggested that the

allocated sample size in each stratum in proportion to the area of the stratum can receive smaller standard errors for producer's and overall accuracies. At the same time, the comprise between user's versus producer's and overall accuracies should be considered by increasing the sample size in the rare classes (Olofsson et al., 2014). Non red cedar forest types occupied much larger areas than red cedar forests, therefore we collected more ROIs for non red cedar forests and increased the ROIs proportion of red cedar forests for good practices. The ROIs were collected manually through visual interpretation based on ground-reference photos and VHSR images in winter from GE. The validation ROIs were digitized after 1995, due to the available GE images in winter within the study area beginning in 1995. We collected validation ROIs for the year 2010 and three time periods of the late 1990s, early 2000s, and late 2000s. We acquired plots/pixels of red cedar and non red cedar forests of 24/5072 and 43/7326 in 2010, 44/4877 and 34/6853 over 2005–2010, 48/3546 and 37/5527 over 2000–2004, and 27/2829 and 38/4734 over 1995–1999, respectively. The ROIs of these four periods have different spatial distributions determined by the locations of the available GE images (Fig. S9a–d). Fig. S9e,f show the zoom-in landscapes of red cedar and non red cedar forests in winter from GE images. These ROIs were used to assess the accuracy of the red cedar maps in different periods. We calculated the adjusted accuracies and area estimates with 95% confidence intervals using the methods presented by Olofsson et al. (2013).

2.5. Comparison with other available red cedar datasets

The Oklahoma Ecological System Mapping (OKESM) project was launched in 2012, and finished by the summer of 2015 (Diamond and Elliott, 2015). The OKESM map was produced to describe the current statewide vegetation distribution. This product was created based on multiple data sources of remote sensing, digital soils, slope, and streams using a decision tree classification approach. The remote sensing images used for the OKESM map were between Dec. 2010 and Aug. 2011 for the eastern regions of Oklahoma, and between Apr. 2013 and Jan. 2014 for

the western regions of Oklahoma. It includes 165 vegetation types with 10 m spatial resolution. The overall user's accuracy was 85%, according to the accuracy assessment with the ground-collected data (Diamond and Elliott, 2015). This product can be downloaded freely from the Oklahoma department of wildlife conservation website (http://www.wildlifedepartment.com/facts_maps/ecoregions.htm).

We compared the 2010 red cedar map (PALSAR/Landsat-RC2010) with the optical image-based OKESM red cedar map in 2015 (OKESM-RC2015). In the OKESM map, the eastern redcedar appeared in multiple vegetation type legends including eastern redcedar forest, woodland, shrubland, and the mixed ecosystems of eastern redcedar and other trees. The OKESM_RC2015 was generated by selecting the vegetation types related to the eastern redcedar forest or woodland. We aggregated the 10 m OKESM-RC2015 two-value map into a 30 m OKESM-RC2015 percentage map. This comparison included two aspects: (1) the spatial distribution of red cedar and (2) the area assessment at the county scale. We visually compared the spatial differences of these two products at 30 m spatial resolution, and analyzed the area

differences by linear regression. The areas were calculated based on these two products at the county level.

3. Results

3.1. The maps of eastern redcedar forest

We mapped *Juniperus virginiana* L. (eastern redcedar) distribution in 2010 and five historical periods from 1984 to 2010. Fig. 8 shows the resultant red cedar forest map (PALSAR/Landsat-RC map) in 2010. This map also shows the non red cedar forest extracted from the 2010 PALSAR-based forest map. The blank areas represented the non-forest areas which were not classified in this study. Within the study area, some counties had clear red cedar encroachment in 2010, including Caddo, Blaine, Dewey, Logan and Payne counties. Fig. 9 shows the resultant red cedar maps during five phases from the late 1980s to the late 2000s, with an interval of five or six years. The forest of other trees

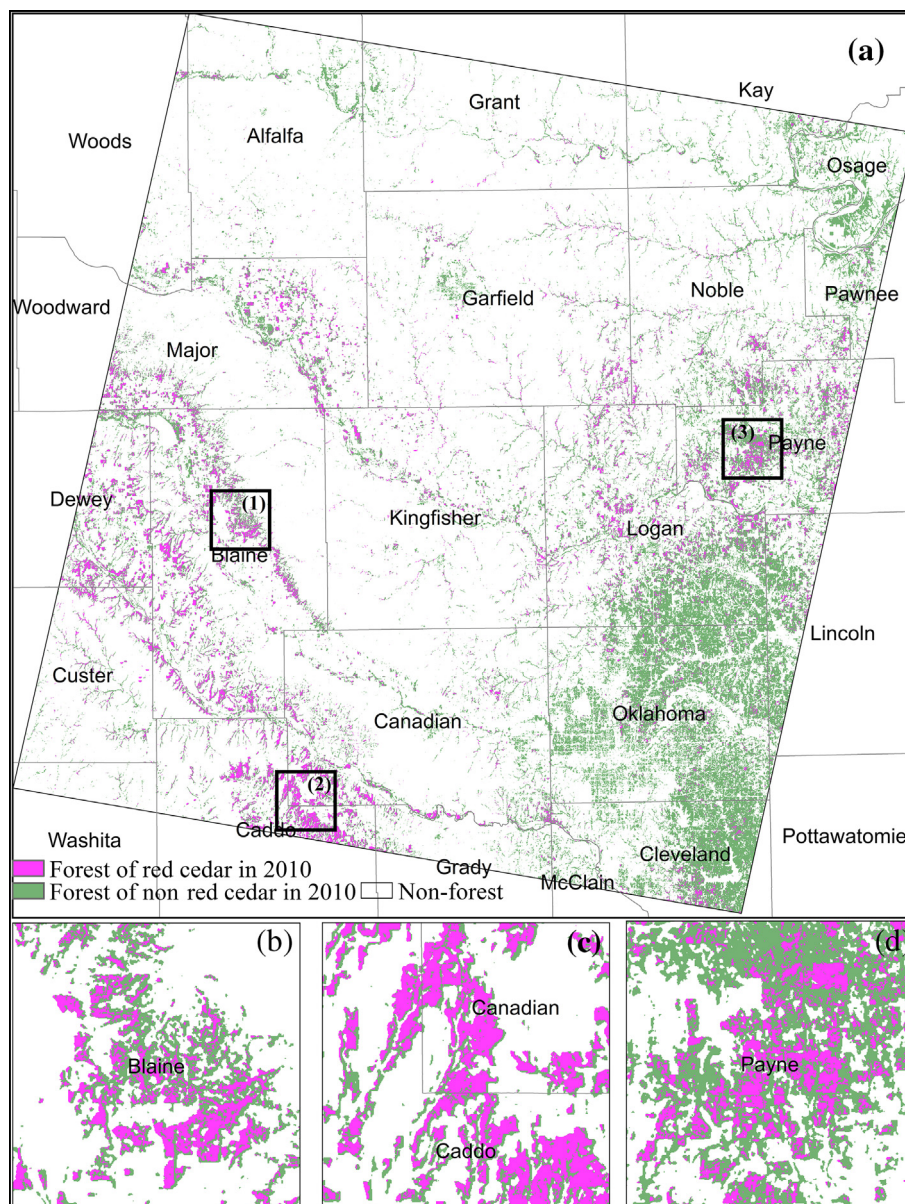


Fig. 8. (a) The red cedar forest map in 2010. (b, c, d) are the zoom-in views of three regions labeled as 1, 2, 3 in (a), respectively. (For interpretation of the references to color in this figure legend, the reader is referred to the web version of this article.)

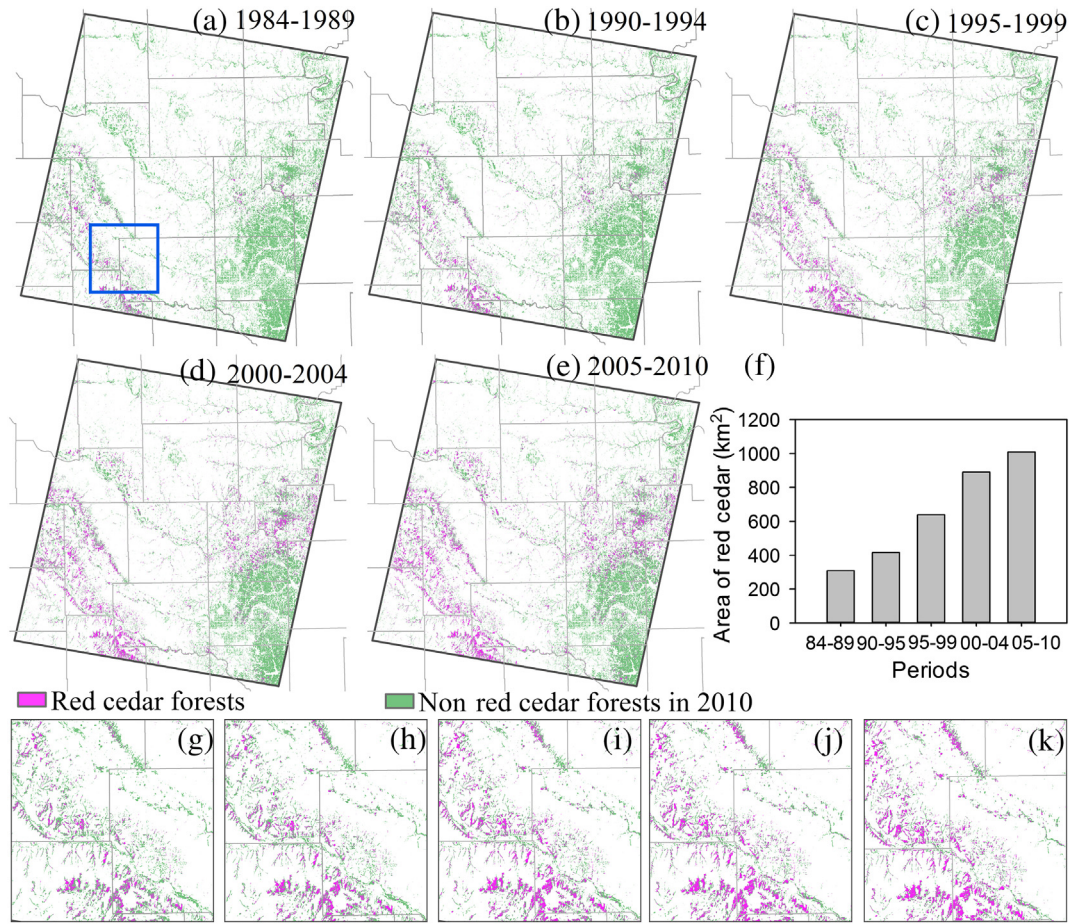


Fig. 9. (a–e) The red cedar forest maps in five periods with 5–6 years as an interval. These maps showed the forest distribution in 2010 derived from the 2010 PALSAR data. (f) The red cedar areas in five different periods, (g–k) shows the zoom-in views for five periods from the late 1980s to the late 2000s for the region highlighted by the blue box in Fig. 9a. (For interpretation of the references to color in this figure legend, the reader is referred to the web version of this article.)

shown in the five epoch maps were extracted from the 2010 PALSAR-based forest map.

3.2. Accuracy assessment

Accuracy assessments of these resultant maps was conducted for 2010 and three time periods of the late 1990s, early 2000s and late 2000s using the validation ROIs introduced in Section 2.4 (Fig. S9). The accuracy of the maps in the late 1980s and early 1990s was not assessed, because the VHSR images for validation from GE were not available until 1995. The assessment results demonstrated that the red cedar and non red cedar maps had reasonably good accuracies (Table 1). The overall accuracies (OA) were 96%, 95%, 94% and 95%, and the Kappa coefficients were 0.91, 0.86, 0.88 and 0.91 in 2010, late 2000s, early 2000s, and late 1990s, respectively. The red cedar category had producer accuracies (PA) of 93%, 90%, 88%, and 90%, and user accuracies (UA) of 97%, 96%, 98%, and 99% in these resultant maps. This result suggested that the red cedar maps in different periods of time were comparable with each other, and it was possible to monitor red cedar encroachment from 1984 to 2010 based on the PALSAR/Landsat-RC maps in the five epochs.

The accuracies of PA, UA and OA were adjusted according to the mapped areas of red cedar and non red cedar forests (Table S1). These maps achieved adjusted OAs of 0.94–0.96. The red cedar type in these maps have adjusted PAs between 0.78 and 0.89, and adjusted UAs between 0.96 and 0.99. We estimated the red cedar forest areas in 2010, late 2000s, early 2000s and late 1990s with 95% confidence interval

margins based on the validation ROIs. The adjusted areas increased from about 811 km² in the late 1990s to 1236 km² in 2010 (Table S1).

3.3. Dynamics of red cedar encroachment and stand age analysis

There was significant red cedar encroachment in the study area from 1984 to 2010 according to the PALSAR/Landsat-RC maps (Fig. 9a–e) and the mapped red cedar area analysis (Fig. 9f). In the late 1980s, red cedar in the study area occupied ~300 km². Then, the red cedar encroached slightly during the early 1990s, reaching an area of ~400 km². The red cedar encroachment mainly happened in the counties of Caddo, Blaine, Dewey and Payne counties during this period. In the late 1990s, the red cedar expanded into Logan, Major and Canadian counties and the area increased to ~600 km². Then, the red cedar continuously encroached in these counties during the 2000s, and the area reached ~900 km² in the early 2000s and ~1000 km² in the late 2000s. The PALSAR/Landsat-RC maps in the five historical time periods showed a continuous encroachment of red cedar, with the most significant encroachment occurring in the late 1990s and early 2000s. During the entire period of 1984–2010, the annual red cedar encroachment rate was about 8%. Further analysis of the geographical patterns of the red cedar encroachment at the county level was presented in supplementary data (text and Fig. S10).

The stand-age map of the red cedar forest in 2010 was generated by overlaying the historical red cedar forest maps in five time periods (Fig. 10a). Fig. 10d shows the percentage distributions of red cedar forest with different stand ages including 1–5 (~20%), 6–10 (~23%), 11–15 (~22%), 16–20 (~11%) and larger than 20 (~24%) years old. Most of

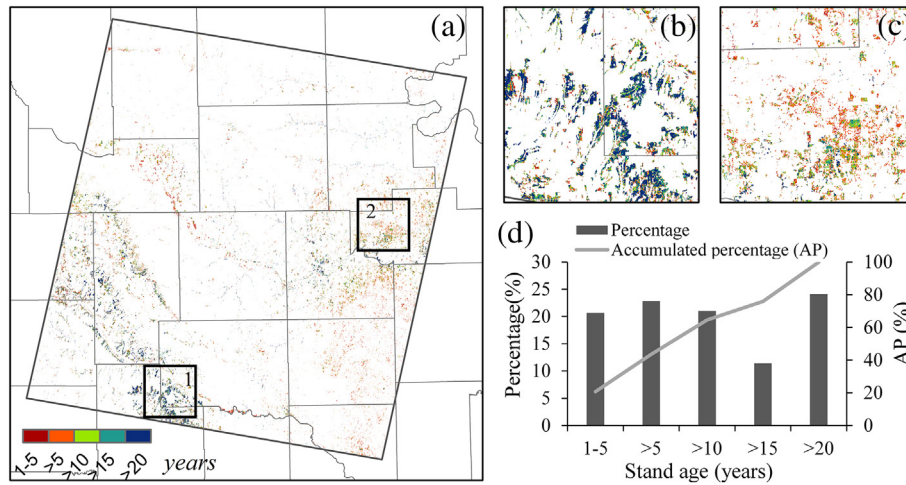


Fig. 10. The stand-age map (a) and two zoom-in views (b, c) for the case regions shown in black boxes of 1, 2 in (a). (d) shows the stand-age histogram of the red cedar forest in 2010. (For interpretation of the references to color in this figure legend, the reader is referred to the web version of this article.)

the red cedar forest (~57%) had a stand age larger than 10 years old, which agreed with the significant red cedar encroachment during the 1990s. 23% of the red cedar forest had a stand age of 6–10 years, and 20% of that had a stand age of <5 years, which coincides with the red cedar encroachment shown in the 2000s.

3.4. A comparison of the PALSAR/Landsat-RC map with the OKESM-RC map

We compared the 2010 PALSAR/Landsat-RC map with the optical image-based red cedar map derived from the OKESM in 2015 (Fig. 11). The spatial distributions of the red cedar in these two maps were visually in high agreement (Fig. 11a and b). The red cedar areas derived from the two maps at county level had a significant linear relationship, with R^2 of 0.93 (Fig. 11c). The slope of 1.34 indicates that there is

moderate difference in red cedar forest area estimates between these two map products for our study area. Therefore, one case region (black boxes in Fig. 11a, b) was selected for zoom-in analysis on these two maps. The red cedar forest distributions derived from the two maps for the case region were shown in Fig. 11d, e. By comparison, we can see some inconsistent patches of red cedar in this case region. Therefore, another zoom-in view (black boxes in Fig. 11d, e) was selected for analysis based on the GE images. Fig. 11f and g show the red cedar distributions (pink areas) in the zoom-in view extracted from the PALSAR/Landsat-RC2010 map and the OKESM-RC2015 map, respectively. The background of Fig. 11f, g used the same image on 03/23/2011 from GE. This zoom-in view comparison revealed that OKESM-RC2015 missed some red cedar forests, which may result in some discrepancies of red cedar area estimations between these two products. The overall

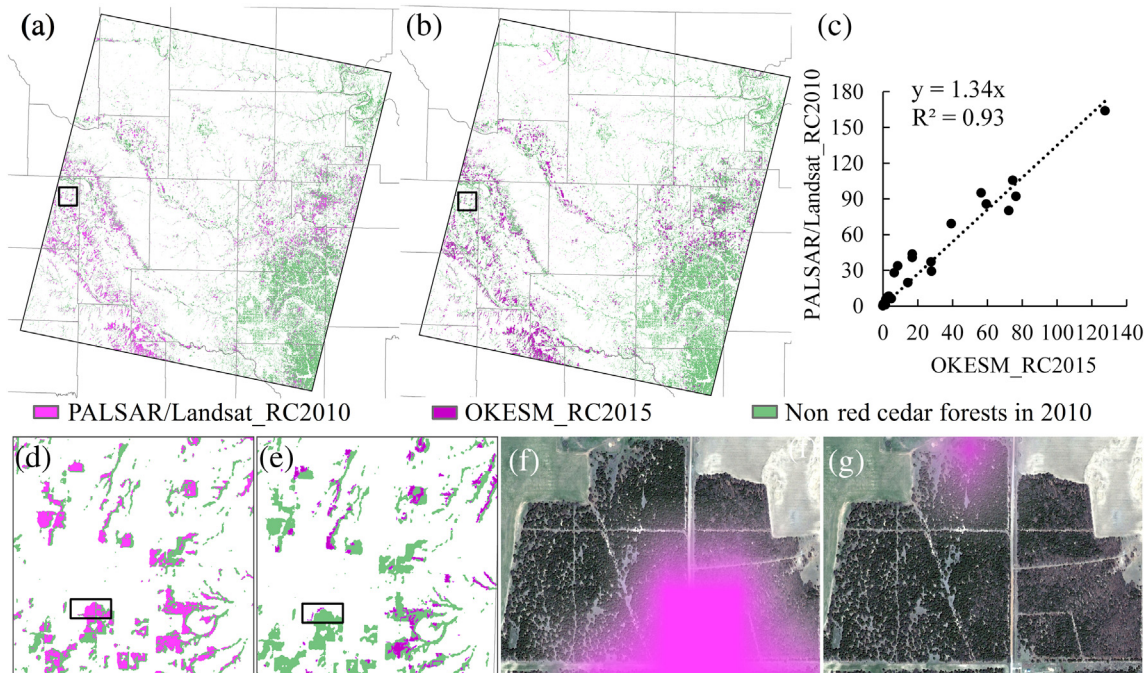


Fig. 11. The comparison of the 2010 red cedar forest map produced in this study (PALSAR/Landsat_RC2010, Fig. 11a) and the red cedar map from the Oklahoma Ecosystem Map in 2015 (OKESM_RC2015, Fig. 11b). (c) Area comparison of PALSAR/Landsat_RC2010 and OKESM_RC2015 at the county level. (d) The zoom-in view of the region shown in black box in Fig. 11a. (e) The zoom-in view of the region shown in black box in Fig. 11b. (f) The zoom-in red cedar map from PALSAR/Landsat_RC2010 for the case region in Fig. 11d. (g) The zoom-in red cedar map from OKESM_RC2015 for the case region in Fig. 11e. The background of Fig. 11f, g was the Google Earth image on 03/23/2011. The pink areas in Fig. 11f, g show the red cedar forests from maps of PALSAR/Landsat_RC2010 and OKESM_RC2015, respectively. (For interpretation of the references to color in this figure legend, the reader is referred to the web version of this article.)

accuracy of 85% was reported for the OKESM map, but the specific accuracy for the red cedar forest in this area is unknown. In addition, the 2010 PALSAR/Landsat-RC map was developed based on the Landsat images from Dec. 2010 to Feb. 2011, while the OKESM-RC map was developed based on the images from 2013 to 2014. A real difference of red cedar forest cover in these two periods may exist, and it could contribute to the inconsistency between these two maps.

4. Discussion

4.1. Source errors of red cedar forest map in 2010 from PALSAR and Landsat images

It is a challenge to classify pixels with mixed vegetation types in land cover mapping or thematic object extractions (Gong et al., 2013; Herold et al., 2008; Sterling and Ducharne, 2008). Considering the red cedar trees within each individual pixel, canopy coverage and tree height determined the classification accuracy in this study. This could be explained by the remote sensing data. The backscatter signals of low frequency SAR (e.g. PALSAR) are related to the three dimensional structures (including crown and height) of forest (Cloude and Papathanassiou, 2003). VIs developed from optical data were more sensitive to the canopy cover (Shimada et al., 2014). These two factors have been confined in most of the forest definitions (FAO, 2012; Friedl et al., 2010; Liu et al., 2005; Qin et al., 2015a; Shimada et al., 2014). However, studies to quantitatively evaluate the roles of these two factors on the classification accuracy at the sub-pixel level are lacking. This study used the FAO definition of forests as lands with tree canopy coverage larger than 10%. The recognition capabilities of 2010 PALSAR/Landsat-RC map at different coverage levels of red cedar canopy in individual pixels is uncertain. The VHRS images from GE and the National Agriculture Imagery Program (NAIP) clearly show tree canopy coverage on the ground surface. We selected three case regions using the simple random design based on these VHRS images, and each region had an extent of about 1 km × 1 km (Fig. 12a). The red cedar canopies were digitalized at individual pixels by visual interpretation based on the GE images in winter (Fig. 12b, Fig. S11). The boundaries of each pixel with shapefile format were obtained by generating a 30 m fishnet based on the PALSAR/Landsat-RC maps. Then, we calculated the coverage of red cedar canopy within each individual pixel, and examined whether the specific pixel was recognized or not in the PALSAR/Landsat-RC maps. Fig. 12c shows the recognition capability of the 2010 PALSAR/Landsat-RC map at different coverage levels of red cedar trees within each pixel. There was 90% probability to recognize the pixels with red cedar coverage higher than 60%, and this probability decreases with decreasing red cedar coverage (Fig. 12c). There was 30% recognition probability in the sparse areas with red cedar canopy coverage ranging 10%–20%. One possible reason was that the unrecognized pixels with red cedar

coverage higher than 10% may have low red cedar height, which cannot be characterized as forests. Another explanation might be that red cedar forests were young with low backscatter signals. Previous studies showed that PALSAR-based forest products had good performance identifying mature forests, but it is possible to omit the sparse and/or low-height forests and woodlands (Qin et al., 2016b; Shimada et al., 2014). If additional data becomes available, further studies will be conducted to evaluate the performance of the PALSAR/Landsat-RC maps with red cedar height, density, or biomass gradients at the sub-pixel scale.

4.2. Uncertainty analysis of red cedar forest maps during 1984–2010

The accuracy of mapping the dynamics of red cedar encroachment into grasslands could be potentially affected by factors within the data and algorithm. It is a challenge to collect good quality data within the phenological window of time to map the annual red cedar distribution and validate the results (Fig. 3, Fig. S2). Although the pixel-based algorithm increased the information input, amounts of pixels were short of sufficient good observations at annual scale, and the data availability showed significant inter-annual variations (Fig. 3, Fig. S2). The quality of input images (Gong et al., 2013) and the uneven availability of Landsat images at temporal and spatial scales (Hansen et al., 2016) posed significant challenges to land cover mapping. Therefore, we produced multi-year red cedar maps in time periods of 5 or 6 years to reduce the uncertainties caused by the data availability.

Accuracy assessments of the red cedar maps had some uncertainties resulting from the limited ground reference data and available VHRS images over time. We only evaluated the red cedar maps in three time periods, the late 1990s, the early 2000s, the late 2000s and the one in 2010. The accuracies of red cedar maps in the late 1980s and the early 1990s were still uncertain, although red cedar distribution patterns agreed with the maps produced by survey questionnaires (Engle et al., 1996). In addition, the spatial distributions of validation ROIs (Fig. S9) for different time periods were confined by the available VHRS images. For example, the ROIs in 2000–2004 (Fig. S9c) were only obtained in the eastern part of the study area, therefore some uncertainties may be caused in the accuracy assessment by the incomprehensively spatial representatives of the validation ROIs.

The phenology feature of red cedar trees having green foliage in the winter is also true for other evergreen trees. Due to the differences from canopy structure, leaf compositions, and phenological phases, the threshold used in this study could exclude some evergreen trees, but could not eliminate the confusions caused by the species with similarly spectral signature (Friedl et al., 2010; Herold et al., 2008). In this study, the commission errors did not affect the resultant maps too much (Table 1), which could be explained by the tree compositions in the grassland ecosystem as discussed in Section 4.3.

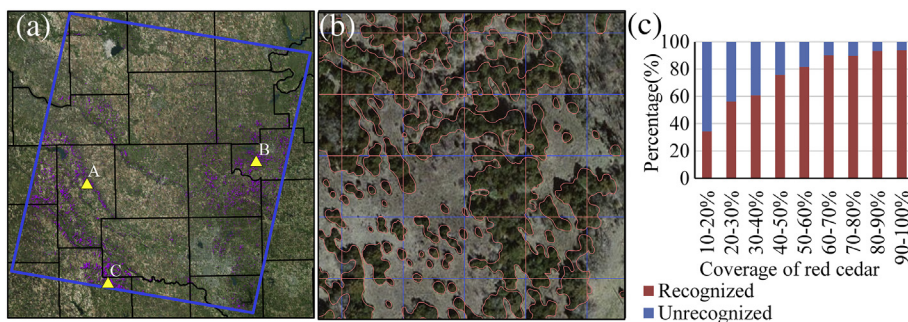


Fig. 12. (a) Spatial distributions of three sample regions with total number of 2838 pixels. The red cedar canopy within each pixel was visually drawn (Fig. S11). (b) The zoom-in visual interpretation of red cedar canopy in each pixel. (c) The percentage of recognized and unrecognized red cedar pixels at different pixel-based red cedar coverage levels. (For interpretation of the references to color in this figure legend, the reader is referred to the web version of this article.)

Table 1
Accuracy assessment of red cedar forest maps based on the validation regions of interests (ROIs) from field photos, and Google Earth images in different periods. More information about the ROIs was shown in Fig. S9.

Periods		Ground truth pixels in each period		Classified pixels	User Accuracy (UA)
		Red cedar	Non red cedar		
2010	Red cedar	4698	141	4839	97%
	Non red cedar	374	7185	7559	95%
	Ground truth pixels	5072	7326	12,398	OA = 96%
	Producer accuracy (PA)	93%	98%		Kappa = 0.91
2005–2010	Red cedar	4402	170	4572	96%
	Non red cedar	475	6683	7153	93%
	Ground truth pixels	4877	6853	11,730	OA = 95%
	Producer accuracy (PA)	90%	98%		Kappa = 0.86
2000–2004	Red cedar	3190	61	3170	98%
	Non red cedar	437	5466	5903	92%
	Ground truth pixels	3546	5527	9073	OA = 94%
	Producer accuracy (PA)	88%	99%		Kappa = 0.88
1995–1999	Red cedar	2553	29	4414	99%
	Non red cedar	276	4705	4407	94%
	Ground truth pixels	2829	4734	8821	OA = 95%
	Producer accuracy (PA)	90%	99%		Kappa = 0.91

4.3. Potential for mapping long-term red cedar encroachment at regional scale

This study presented the potential of mapping the dynamics of red cedar encroachment to grassland at the regional scale through combining PALSAR data and time series Landsat data by using a pixel and phenology-based algorithm. Although the red cedar forest maps in the late 1980s and early 1990s were not validated, these maps showed consistent red cedar distribution with the maps obtained by survey questionnaires in 1985 and 1995 (Engle et al., 1996). These two resultant maps also showed the eastern redcedar expanded along river drainages, which provides remote sensing evidence for the study by Engle et al. (1996). The red cedar forest maps in other periods had reasonable producer accuracies of 88%–93%. The successful practice in this study could be explained by data availability, algorithm, and vegetation types.

The L-band PALSAR images have shown good performance on mapping forest (Shimada et al., 2014) and plantations (Chen et al., 2016; Dong et al., 2013; Miettinen and Liew, 2011). The release of 25 m PALSAR mosaic images offered improved spatial resolution datasets for forest mapping (Shimada et al., 2014). The Landsat data provided a long term (since the 1970s) data source at 30 m spatial resolution for time series analysis (Woodcock et al., 2008; Wulder et al., 2012). Using all good observation data of individual pixels from both the TM and ETM+ images improved the description of phenology information (Dong et al., 2016; Dong et al., 2015) and increased the temporal range of the study. The GEE platform facilitated the collection and processing of all the surface reflectance data from 1984 to 2011. A recent study on paddy rice mapping has shown the efficient capability of the GEE platform for the land cover mapping based on thousands of images (Dong et al., 2016).

The different phenological characteristics between red cedar trees and other trees (e.g. oaks) in the study area could be represented by vegetation indices of NDVI/EVI/LSWI (Figs. 5, 6). For example, in the winter, the red cedar trees have canopies with green leaves, while other dominant trees have significant defoliation. Thus, the red cedar can be identified effectively with the images in the winter. Based on this analysis, this study proposed the pixel- and phenology-based algorithm with all good observations of Landsat 5/7 at a given pixel as input. This algorithm has better potential for time series analysis than traditional image- and statistics-based algorithms for two major reasons: (1) pixel-based algorithms increase the data input to describe the phenology (Fig. S2), and (2) phenology-based algorithms can be used repeatedly at a given area with similar climate and ecosystem types over time (Dong et al., 2015; Zhong et al., 2014).

Deciduous forest and prairies, which include tall, mixed, and short grasses, are two plant communities in western Oklahoma (Bruner, 1931). This study examined the dynamics of red cedar encroachment into native grasslands in the ecotone between deciduous forests and grass prairie. Red cedar trees had unique phenology spectra which differed from that of the dominant deciduous trees. Therefore, the phenological characteristics of red cedar and deciduous trees could be successfully used to map the red cedar forest in grassland regions by remote sensing images using the phenology-based algorithm in this study.

4.4. Implications for extensive applications and future development

To our knowledge, this is the first attempt to monitor the dynamics of red cedar encroachment to native grasslands using remote sensing approaches at the regional scale. The pixel- and phenology-based algorithm based on PALSAR and time series Landsat images may have the potential to be applied widely (1) to other grassland regions, and (2) to extract other invasive tree species by adjusting the threshold used in this study. Detailed and long-term red cedar maps provide important data sources for the management of grasslands, and for the exploring of causes and consequences of woody plant encroachment at the regional scale (Barger et al., 2011; Gavier-Pizarro et al., 2012; Ge and Zou, 2013; Turner et al., 2003). Currently, this work was limited at both the spatial extent and the temporal range. We will apply this approach to map the dynamics of red cedar encroachment across the grasslands in Oklahoma and the Southern Great Plains. The release of the PALSAR2 data (Shimada et al., 2014) provides an opportunity to map the red cedar patterns after 2010. Limited by the quality and quantity of the input data, this study produced the multi-year red cedar maps. The annual red cedar time series maps could be generated in the future through improving the mapping algorithms and using more data sources (e.g. Landsat 8, Sentinel-2).

5. Conclusions

Woody plant encroachment is occurring globally in multiple ecosystems, especially in the grassland of the southern great plains of the USA. The lack of long-term red cedar maps at the regional scale severely limits our understanding of the ecosystem and climate feedbacks on woody plant encroachment, rangeland management and biodiversity conservation. Landsat data provided the possibility to trace back the regional land cover changes to the 1980s at 30 m spatial resolution. This study integrated 4233 Landsat 5/7 images from 1984 to 2010 with the

PALSAR data in 2010 to monitor the red cedar dynamics in the central region of Oklahoma by a pixel and phenology-based algorithm. The Landsat-based time series vegetation indices can capture the phenological differences of red cedar and other trees, which facilitated the red cedar mapping in this study. The moderate spatial resolution images of Landsat and PALSAR had good performance to identify the regions with red cedar coverage larger than 50%, and the identification capability reduced with the decreasing of red cedar coverage. The uneven image qualities at spatial and temporal scales and algorithm could cause some uncertainties that occurred on the resultant red cedar maps. Further studies are needed to apply this pixel- and phenology-based algorithm using PALSAR and time series Landsat images to other grassland regions.

Acknowledgments

This study was supported by research grants through the USDA National Institute of Food and Agriculture (NIFA) (2013-69002 and 2016-68002-24967) and the US National Science Foundation EPSCoR program (IIA-1301789). We thank the anonymous reviewers for their constructive comments and suggestions of earlier version of the manuscript.

Appendix A. Supplementary data

Supplementary data to this article can be found online at <http://dx.doi.org/10.1016/j.rse.2016.12.025>.

References

- Anderson, J.J., Cobb, N.S., 2004. Tree cover discrimination in panchromatic aerial imagery of pinyon-juniper woodlands. *Photogramm. Eng. Remote Sens.* 70, 1063–1068.
- Archer, S., Vavra, M., Laycock, W., Pieper, R., 1994. Woody plant encroachment into southwestern grasslands and savannas: rates, patterns and proximate causes. *Ecological Implications of Livestock Herbivory in the West*. Society for Range Management, pp. 13–68.
- Baghdadi, N., Boyer, N., Todoroff, P., El Hajj, M., Begue, A., 2009. Potential of SAR sensors TerraSAR-X, ASAR/ENVISAT and PALSAR/ALOS for monitoring sugarcane crops on Reunion Island. *Remote Sens. Environ.* 113, 1724–1738.
- Barger, N.N., Archer, S.R., Campbell, J.L., Huang, C.Y., Morton, J.A., Knapp, A.K., 2011. Woody plant proliferation in North American drylands: A synthesis of impacts on ecosystem carbon balance. *J. Geophys. Res. Biogeosci.* 116.
- Briggs, J.M., Knapp, A.K., Blair, J.M., Heisler, J.L., Hoch, G.A., Lett, M.S., McCARRON, J.K., 2005. An ecosystem in transition: causes and consequences of the conversion of mesic grassland to shrubland. *Bioscience* 55, 243–254.
- Bruner, W.E., 1931. The vegetation of Oklahoma. *Ecol. Monogr.* 1, 100–188.
- Caterina, G.L., Will, R.E., Turton, D.J., Wilson, D.S., Zou, C.B., 2014. Water use of *Juniperus virginiana* trees encroached into mesic prairies in Oklahoma, USA. *Ecohydrology* 7, 1124–1134.
- Chen, B., Li, X., Xiao, X., Zhao, B., Dong, J., Kou, W., Qin, Y., Yang, C., Wu, Z., Sun, R., 2016. Mapping tropical forests and deciduous rubber plantations in Hainan Island, China by integrating PALSAR 25-m and multi-temporal Landsat images. *Int. J. Appl. Earth Obs. Geoinf.* 50, 117–130.
- Clark, M.L., Roberts, D.A., Clark, D.B., 2005. Hyperspectral discrimination of tropical rain forest tree species at leaf to crown scales. *Remote Sens. Environ.* 96, 375–398.
- Cloude, S.R., Papathanassiou, K.P., 2003. Three-stage inversion process for polarimetric SAR interferometry. *IEE Proceedings-Radar Sonar and Navigation*, 150, pp. 125–134.
- DeSantis, R.D., Hallgren, S.W., Lynch, T.B., Burton, J.A., Palmer, M.W., 2010. Long-term directional changes in upland Quercus forests throughout Oklahoma, USA. *J. Veg. Sci.* 21, 606–615.
- DeSantis, R.D., Hallgren, S.W., Stahle, D.W., 2011. Drought and fire suppression lead to rapid forest composition change in a forest-prairie ecotone. *For. Ecol. Manag.* 261, 1833–1840.
- Diamond, D.D., Elliott, L.F., 2015. Oklahoma Ecological Systems Mapping Interpretive Booklet: Methods, Short Type Descriptions, and Summary Results. Oklahoma Department of Wildlife Conservation, Norman.
- Dong, J.W., Xiao, X.M., Sheldon, S., Biradar, C., Duong, N.D., Hazarika, M., 2012a. A comparison of forest cover maps in Mainland Southeast Asia from multiple sources: PALSAR, MERIS, MODIS and FRA. *Remote Sens. Environ.* 127, 60–73.
- Dong, J.W., Xiao, X.M., Sheldon, S., Biradar, C., Xie, G.S., 2012b. Mapping tropical forests and rubber plantations in complex landscapes by integrating PALSAR and MODIS imagery. *ISPRS J. Photogramm. Remote Sens.* 74, 20–33.
- Dong, J.W., Xiao, X.M., Chen, B.Q., Torbick, N., Jin, C., Zhang, G.L., Biradar, C., 2013. Mapping deciduous rubber plantations through integration of PALSAR and multi-temporal Landsat imagery. *Remote Sens. Environ.* 134, 392–402.
- Dong, J.W., Xiao, X.M., Kou, W.L., Qin, Y.W., Zhang, G.L., Li, L., Jin, C., Zhou, Y.T., Wang, J., Biradar, C., Liu, J.Y., Moore, B., 2015. Tracking the dynamics of paddy rice planting area in 1986–2010 through time series Landsat images and phenology-based algorithms. *Remote Sens. Environ.* 160, 99–113.
- Dong, J., Xiao, X., Menarguez, M.A., Zhang, G., Qin, Y., Thau, D., Biradar, C., Moore, B., 2016. Mapping paddy rice planting area in northeastern Asia with Landsat 8 images, phenology-based algorithm and Google Earth Engine. *Remote Sens. Environ.* 185, 142–154.
- Engle, D.M., Bidwell, T.G., Moseley, M.E., 1996. Invasion of Oklahoma Rangelands and Forests by Eastern Redcedar and Ashe Juniper. Oklahoma Cooperative Extension Service, Division of Agricultural Sciences and Natural Resources, Oklahoma State University.
- Falkowski, M.J., Smith, A.M.S., Hudak, A.T., Gessler, P.E., Vierling, L.A., Crookston, N.L., 2006. Automated estimation of individual conifer tree height and crown diameter via two-dimensional spatial wavelet analysis of lidar data. *Can. J. Remote Sens.* 32, 153–161.
- FAO, 2012. Forest Resources Assessments (FRA2010). Food and Agricultural Organization of the United Nations, Rome.
- Friedl, M.A., Sulla-Menashe, D., Tan, B., Schneider, A., Ramankutty, N., Sibley, A., Huang, X.M., 2010. MODIS Collection 5 global land cover: Algorithm refinements and characterization of new datasets. *Remote Sens. Environ.* 114, 168–182.
- Gavier-Pizarro, G.L., Kuemmerle, T., Hoyos, L.E., Stewart, S.I., Huebner, C.D., Keuler, N.S., Radeloff, V.C., 2012. Monitoring the invasion of an exotic tree (*Ligustrum lucidum*) from 1983 to 2006 with Landsat TM/ETM plus satellite data and Support Vector Machines in Cordoba, Argentina. *Remote Sens. Environ.* 122, 134–145.
- Ge, J.J., Zou, C., 2013. Impacts of woody plant encroachment on regional climate in the southern Great Plains of the United States. *J. Geophys. Res.-Atmos.* 118, 9093–9104.
- Gong, P., Wang, J., Yu, L., Zhao, Y.C., Zhao, Y.Y., Liang, L., Niu, Z.G., Huang, X.M., Fu, H.H., Liu, S., Li, C.C., Li, X.Y., Fu, W., Liu, C.X., Xu, Y., Wang, X.Y., Cheng, Q., Hu, L.Y., Yao, W.B., Zhang, H., Zhu, P., Zhao, Z.Y., Zhang, H.Y., Zheng, Y.M., Ji, L.Y., Zhang, Y.W., Chen, H., Yan, A., Guo, J.H., Yu, L., Wang, L., Liu, X.J., Shi, T.T., Zhu, M.H., Chen, Y.L., Yang, G.W., Tang, P., Xu, B., Giri, C., Clinton, N., Zhu, Z.L., Chen, J., Chen, J., 2013. Finer resolution observation and monitoring of global land cover: first mapping results with Landsat TM and ETM+ data. *Int. J. Remote Sens.* 34, 2607–2654.
- Hansen, M.C., Potapov, P.V., Goetz, S.J., Turubanova, S., Tyukavina, A., Krylov, A., Kommareddy, A., Egorov, A., 2016. Mapping tree height distributions in Sub-Saharan Africa using Landsat 7 and 8 data. *Remote Sens. Environ.* 185, 221–232.
- Hennessy, J.T., Gibbens, R.P., Tromble, J.M., Cardenas, M., 1983. Vegetation changes from 1935 to 1980 in Mesquite Dunelands and former grasslands of Southern New-Mexico. *J. Range Manag.* 36, 370–374.
- Herold, M., Mayaux, P., Woodcock, C.E., Baccini, A., Schmullius, C., 2008. Some challenges in global land cover mapping: an assessment of agreement and accuracy in existing 1 km datasets. *Remote Sens. Environ.* 112, 2538–2556.
- Hoagland, B., 2000. The vegetation of Oklahoma: a classification for landscape mapping and conservation planning. *Southwest. Nat.* 45, 385–420.
- Huete, A., Didan, K., Miura, T., Rodriguez, E.P., Gao, X., Ferreira, L.G., 2002. Overview of the radiometric and biophysical performance of the MODIS vegetation indices. *Remote Sens. Environ.* 83, 195–213.
- Inglis, J.M., 1964. A History of Vegetation on the Rio Grande Plain. Texas Parks and Wildlife Department.
- Johnson, F.L., Risser, P.G., 1975. A quantitative comparison between an oak forest and an oak savannah in central Oklahoma. *Southwest. Nat.* 75–84.
- Lehmann, E.A., Caccetta, P., Lowell, K., Mitchell, A., Zhou, Z.-S., Held, A., Milne, T., Tapley, I., 2015. SAR and optical remote sensing: Assessment of complementarity and interoperability in the context of a large-scale operational forest monitoring system. *Remote Sens. Environ.* 156, 335–348.
- Liu, J.Y., Liu, M.L., Tian, H.Q., Zhuang, D.F., Zhang, Z.X., Zhang, W., Tang, X.M., Deng, X.Z., 2005. Spatial and temporal patterns of China's cropland during 1990–2000: An analysis based on Landsat TM data. *Remote Sens. Environ.* 98, 442–456.
- Loveland, T.R., Reed, B.C., Brown, J.F., Ohlen, D.O., Zhu, Z., Yang, L., Merchant, J.W., 2000. Development of a global land cover characteristics database and IGBP DISCover from 1 km AVHRR data. *Int. J. Remote Sens.* 21, 1303–1330.
- Martin, M.E., Newman, S.D., Aber, J.D., Congalton, R.G., 1998. Determining forest species composition using high spectral resolution remote sensing data. *Remote Sens. Environ.* 65, 249–254.
- Masek, J.G., Vermote, E.F., Saleous, N.E., Wolfe, R., Hall, F.G., Huemmrich, K.F., Gao, F., Kutler, J., Lim, T.K., 2006. A Landsat surface reflectance dataset for North America, 1990–2000. *IEEE Geosci. Remote Sens. Lett.* 3, 68–72.
- Miettinen, J., Liew, S.C., 2011. Separability of insular Southeast Asian woody plantation species in the 50 m resolution ALOS PALSAR mosaic product. *Remote Sens. Lett.* 2, 299–307.
- Mueller, H., Rufin, P., Griffiths, P., Siqueira, A.J.B., Hostert, P., 2015. Mining dense Landsat time series for separating cropland and pasture in a heterogeneous Brazilian savanna landscape. *Remote Sens. Environ.* 156, 490–499.
- Myster, R.W., 2009. Tree seedling survivorship, growth, and allocation in the cross timbers ecotone of Oklahoma, USA. *Plant Ecol.* 205, 193–199.
- Olofsson, P., Foody, G.M., Stehman, S.V., Woodcock, C.E., 2013. Making better use of accuracy data in land change studies: estimating accuracy and area and quantifying uncertainty using stratified estimation. *Remote Sens. Environ.* 129, 122–131.
- Olofsson, P., Foody, G.M., Herold, M., Stehman, S.V., Woodcock, C.E., Wulder, M.A., 2014. Good practices for estimating area and assessing accuracy of land change. *Remote Sens. Environ.* 148, 42–57.
- Poznanovic, A.J., Falkowski, M.J., Maclean, A.L., Smith, A.M.S., Evans, J.S., 2014. An accuracy assessment of tree detection algorithms in Juniper woodlands. *Photogramm. Eng. Remote Sens.* 80, 627–637.
- Pu, R.L., Landry, S., 2012. A comparative analysis of high spatial resolution IKONOS and WorldView-2 imagery for mapping urban tree species. *Remote Sens. Environ.* 124, 516–533.

- Qin, Y., Xiao, X., Dong, J., Zhang, G., Shimada, M., Liu, J., Li, C., Kou, W., Moore, B., 2015a. Forest cover maps of China in 2010 from multiple approaches and data sources: PALSAR, Landsat, MODIS, FRA, and NFI. *ISPRS J. Photogramm. Remote Sens.* 109, 1–16.
- Qin, Y.W., Xiao, X.M., Dong, J.W., Zhou, Y.T., Zhu, Z., Zhang, G.L., Du, G.M., Jin, C., Kou, W.L., Wang, J., Li, X.P., 2015b. Mapping paddy rice planting area in cold temperate climate region through analysis of time series Landsat 8 (OLI), Landsat 7 (ETM+) and MODIS imagery. *ISPRS J. Photogramm. Remote Sens.* 105, 220–233.
- Qin, Y., Xiao, X., Wang, J., Dong, J., Ewing, K., Hoagland, B., Hough, D., Fagin, T., Zou, Z., Geissler, G., Xian, G., Loveland, T., 2016a. Mapping annual forest cover in sub-humid and semi-arid regions through analysis of Landsat and PALSAR imagery. *Remote Sens.* 8, 933.
- Qin, Y.W., Xiao, X.M., Dong, J.W., Zhang, G.L., Roy, P.S., Joshi, P.K., Gilani, H., Murthy, M.S.R., Jin, C., Wang, J., Zhang, Y., Chen, B.Q., Menarguez, M.A., Biradar, C.M., Bajgain, R., Li, X.P., Dai, S.Q., Hou, Y., Xin, F.F., Moore, B., 2016b. Mapping forests in monsoon Asia with ALOS PALSAR 50-m mosaic images and MODIS imagery in 2010. *Sci. Rep.* 6.
- Rice, E.L., Penfound, W.T., 1959. The upland forests of Oklahoma. *Ecology* 40, 593–608.
- Sankey, T., Glenn, N., 2011. Landsat-5 TM and lidar fusion for sub-pixel Juniper tree cover estimates in a western rangeland. *Photogramm. Eng. Remote Sens.* 77, 1241–1248.
- Shimada, M., Ohtaki, T., 2010. Generating large-scale high-quality SAR mosaic datasets: application to PALSAR data for global monitoring. *IEEE J. Sel. Top. Appl. Earth Obs. Remote Sens.* 3, 637–656.
- Shimada, M., Isoguchi, O., Tadono, T., Isono, K., 2009. PALSAR radiometric and geometric calibration. *IEEE Trans. Geosci. Remote Sens.* 47, 3915–3932.
- Shimada, M., Itoh, T., Motooka, T., Watanabe, M., Shiraishi, T., Thapa, R., Lucas, R., 2014. New global forest/non-forest maps from ALOS PALSAR data (2007–2010). *Remote Sens. Environ.* 155, 13–31.
- Sterling, S., Ducharme, A., 2008. Comprehensive data set of global land cover change for land surface model applications. *Glob. Biogeochem. Cycles* 22.
- Strand, E.K., Smith, A.M.S., Bunting, S.C., Vierling, L.A., Hann, D.B., Gessler, P.E., 2006. Wavelet estimation of plant spatial patterns in multitemporal aerial photography. *Int. J. Remote Sens.* 27, 2049–2054.
- Tucker, C.J., 1979. Red and photographic infrared linear combinations for monitoring vegetation. *Remote Sens. Environ.* 8, 127–150.
- Turner, W., Spector, S., Gardiner, N., Fladeland, M., Sterling, E., Steininger, M., 2003. Remote sensing for biodiversity science and conservation. *Trends Ecol. Evol.* 18, 306–314.
- Urbazaev, M., Thiel, C., Mathieu, R., Naidoo, L., Levick, S.R., Smit, I.P., Asner, G.P., Schmullius, C., 2015. Assessment of the mapping of fractional woody cover in southern African savannas using multi-temporal and polarimetric ALOS PALSAR L-band images. *Remote Sens. Environ.* 166, 138–153.
- Van Auken, O.W., 2000. Shrub invasions of north American semiarid grasslands. *Annu. Rev. Ecol. Syst.* 31, 197–215.
- Vermote, E.F., ElSaleous, N., Justice, C.O., Kaufman, Y.J., Privette, J.L., Remer, L., Roger, J.C., Tanre, D., 1997. Atmospheric correction of visible to middle-infrared EOS-MODIS data over land surfaces: Background, operational algorithm and validation. *J. Geophys. Res.-Atmos.* 102, 17131–17141.
- Wang, J., Xiao, X.M., Qin, Y.W., Dong, J.W., Zhang, G.L., Kou, W.L., Jin, C., Zhou, Y.T., Zhang, Y., 2015. Mapping paddy rice planting area in wheat-rice double-cropped areas through integration of Landsat-8 OLI, MODIS, and PALSAR images. *Sci. Rep.* 5 (Article number: 10088).
- Waser, L.T., Baltasvias, E., Ecker, K., Eisenbeiss, H., Feldmeyer-Christe, E., Ginzler, C., Kuchler, M., Zhang, L., 2008. Assessing changes of forest area and shrub encroachment in a mire ecosystem using digital surface models and CIR aerial images. *Remote Sens. Environ.* 112, 1956–1968.
- Williams, R.J., Hallgren, S.W., Wilson, G.W.T., Palmer, M.W., 2013. *Juniperus virginiana* Encroachment into upland oak forests alters arbuscular mycorrhizal abundance and litter chemistry. *Appl. Soil Ecol.* 65, 23–30.
- Woodcock, C.E., Allen, R., Anderson, M., Belward, A., Bindschadler, R., Cohen, W., Gao, F., Goward, S.N., Helder, D., Helmer, E., Nemani, R., Oreopoulos, L., Schott, J., Thenkabail, P.S., Vermote, E.F., Vogelmann, J., Wulder, M.A., Wynne, R., Team, L.S., 2008. Free access to Landsat imagery. *Science* 320, 1011.
- Woods, A., Omernik, J., Butler, D., Ford, J., Henley, J., Hoagland, B., Arndt, D., Moran, B., 2005. Ecoregions of Oklahoma (color poster with map, descriptive text, summary tables, and photographs). US Geological Survey (Map Scale 1: 1,250,000), Reston, Virginia.
- Wulder, M.A., White, J.C., Goward, S.N., Masek, J.G., Irons, J.R., Herold, M., Cohen, W.B., Loveland, T.R., Woodcock, C.E., 2008. Landsat continuity: issues and opportunities for land cover monitoring. *Remote Sens. Environ.* 112, 955–969.
- Wulder, M.A., Masek, J.G., Cohen, W.B., Loveland, T.R., Woodcock, C.E., 2012. Opening the archive: how free data has enabled the science and monitoring promise of Landsat. *Remote Sens. Environ.* 122, 2–10.
- Wulder, M.A., White, J.C., Loveland, T.R., Woodcock, C.E., Belward, A.S., Cohen, W.B., Fosnight, E.A., Shaw, J., Masek, J.G., Roy, D.P., 2016. The global Landsat archive: Status, consolidation, and direction. *Remote Sens. Environ.* 185, 271–283.
- Xiao, X.M., Hollinger, D., Aber, J., Goltz, M., Davidson, E.A., Zhang, Q.Y., Moore, B., 2004. Satellite-based modeling of gross primary production in an evergreen needle leaf forest. *Remote Sens. Environ.* 89, 519–534.
- Xiao, X.M., Boles, S., Liu, J.Y., Zhuang, D.F., Frolking, S., Li, C.S., Salas, W., Moore, B., 2005. Mapping paddy rice agriculture in southern China using multi-temporal MODIS images. *Remote Sens. Environ.* 95, 480–492.
- Xiao, X., Hagen, S., Zhang, Q., Keller, M., Moore, B., 2006. Detecting leaf phenology of seasonally moist tropical forests in South America with multi-temporal MODIS images. *Remote Sens. Environ.* 103, 465–473.
- Xiao, X., Dorovskoy, P., Biradar, C., Bridge, E., 2011. A library of georeferenced photos from the field. *Eos. Trans. AGU* 92, 453–454.
- Yang, J., Weisberg, P.J., Bristow, N.A., 2012. Landsat remote sensing approaches for monitoring long-term tree cover dynamics in semi-arid woodlands: comparison of vegetation indices and spectral mixture analysis. *Remote Sens. Environ.* 119, 62–71.
- Zhong, L.H., Gong, P., Biging, G.S., 2014. Efficient corn and soybean mapping with temporal extendability: A multi-year experiment using Landsat imagery. *Remote Sens. Environ.* 140, 1–13.
- Zhu, Z., Woodcock, C.E., 2012. Object-based cloud and cloud shadow detection in Landsat imagery. *Remote Sens. Environ.* 118, 83–94.
- Zou, C.B., Qiao, L., Wilcox, B.P., 2016. Woodland expansion in central Oklahoma will significantly reduce streamflows - a modelling analysis. *Ecology* 9, 807–816.